

Anatomy of Empirical Transit Spectra of Mars based on TGO/NOMAD

SHOHEI AOKI ^{1, 2, *} YUKA FUJII ^{3, 4, 5, *} HIDEO SAGAWA ⁶ GERONIMO L. VILLANUEVA ⁷ IAN THOMAS ⁸
 BOJAN RISTIC,⁸ FRANK DAERDEN ⁸ MIGUEL ANGEL LÓPEZ-VALVERDE ⁹ MANISH R. PATEL ¹⁰ JONATHON MASON ¹⁰,
 YANNICK WILLAME ⁸ GIANCARLO BELLUCCI ¹¹ AND ANN CARINE VANDAELE ⁸

¹*Department of Complexity Science and Engineering, Graduate School of Frontier Sciences, The University of Tokyo, 5-1-5 Kashiwanoha, Kashiwa, Chiba 277- 8561, Japan*

²*Department of Geophysics, Graduate School of Science, Tohoku University, Sendai, Miyagi 980-8578, Japan*

³*Division of Science, National Astronomical Observatory of Japan, 2-21-1 Osawa, Mitaka, Tokyo 181-8588, Japan*

⁴*Graduate Institute for Advanced Studies, SOKENDAI, 2-21-1 Osawa, Mitaka, Tokyo 181-8588, Japan*

⁵*Department of Earth and Planetary Science, University of Tokyo, 7-3-1 Hongo, Bunkyo-ku, Tokyo 113-0033, Japan*

⁶*Faculty of Science, Kyoto Sangyo University, Kamigamo Motoyama, Kita-ku, Kyoto 603-8555, Japan*

⁷*NASA Goddard Space Flight Center, 8800 Greenbelt Rd., Greenbelt, 20771 MD, USA*

⁸*Royal Belgian Institute for Space Aeronomy, 3 Avenue Circulaire, 1180 Brussels, Belgium*

⁹*Instituto de Astrofísica de Andalucía, Glorieta de la Astronomía, 18008 Granada, Spain*

¹⁰*Department of Physical Sciences, The Open University, Milton Keynes, MK7 6AA, UK*

¹¹*Istituto di Astrofisica e Planetologia Spaziali, Via del Fosso del Cavaliere 100, Roma, Italy*

ABSTRACT

Transit spectroscopy is a powerful tool for probing atmospheric structures of exoplanets. Accurately accounting for the effects of aerosols is key to reconstructing atmospheric properties from transit spectra, yet this remains a significant challenge. To advance this effort, it is invaluable to examine the spectral features of well-characterized planetary atmospheres. Here, we synthesize empirical transit spectra of Mars across different seasons based on data from the NOMAD’s Solar Occultation channel onboard ExoMars/TGO, which operates at wavelengths of 0.2–0.65 and 2–4 μm . In the generated empirical transit spectra, the atmosphere below 25 km is found to be largely opaque due to the presence of micron-sized dust and H_2O ice clouds, both of which substantially weaken spectral features. The spectra exhibit CO_2 absorption features at 2.7–2.8 μm and signatures of sub-micron-sized mesospheric H_2O ice clouds around 3.1 μm , accompanied by a continuum slope. The amplitudes of these spectral features are found to vary with the Martian seasons, where the dust storms weaken the CO_2 signatures and strengthen the H_2O ice features, which serve as potential indicators of a dusty planet like Mars. If TRAPPIST-1f possessed a Mars-like atmospheric structure, both CO_2 and H_2O ice features would be detectable at a noise level of 3 ppm, a level likely beyond current observational capabilities. Nevertheless, the 3.1 μm feature produced by sub-micron-sized mesospheric H_2O ice clouds offers a novel avenue for characterizing the atmospheres of habitable-zone exoplanets.

Keywords: Exoplanet atmospheres (487) — Extrasolar rocky planets (511) — Habitable planets (695) — Interdisciplinary astronomy (804) — Exoplanet atmospheric dynamics (2307)

1. INTRODUCTION

Characterization of rocky planets is one of the central interests in exoplanet research. It is essential for both comparative planetology and astrobiological investigations beyond the Solar System. A promising method for studying their atmospheres is transit spectroscopy. The James Webb Space Telescope (JWST) has begun performing transit spectroscopy of exoplanets smaller than Neptune. It has detected several atmospheric species, including CH₄ and CO₂, in cool sub-Neptunes, and has even hinted at the presence of some unexpected species (Holmberg & Madhusudhan 2024; Madhusudhan et al. 2025). Transit spectroscopy of Earth-sized planets around low-mass stars has also been attempted, although molecular signatures have not been clearly constrained (e.g., Lim et al. 2023; Barclay et al. 2025). In the near future, next-generation ground-based extremely large telescopes are also expected to carry out the search for atmospheric species in Earth-sized planets orbiting nearby low-mass stars.

Nevertheless, reconstructing the properties of an exoplanetary atmosphere from its transit spectrum remains a challenge. While technical limitations such as low signal-to-noise ratios, limited spectral resolution, and restricted wavelength coverage pose clear obstacles, fundamental difficulties persist even under idealized, noise-free conditions. In particular, the impact of liquid/solid particles (e.g., clouds, aerosols, and dust) on transit spectra, as well as the interpretation of their spectral features, remains a challenge in exoplanetary characterization. The abundance and properties of the condensates, along with those of their gaseous precursors, can vary both spatially and temporally through complex interactions with atmospheric dynamics, making it difficult to model them self-consistently and to incorporate their effects into data analysis. One-dimensional atmospheric models that are used to simulate or interpret transit spectra often simplify these complexities. A substantial number of previous works that provided modeled transit spectra of a variety of rocky planets have typically neglected these condensates or assumed ad hoc properties for them, which may not adequately capture the diversity of real atmospheres. More recently, transit spectra based on three-dimensional general circulation models have also been modeled (e.g., Kopparapu et al. 2017; Fujii et al. 2017; Fauchez et al. 2019). However, due to uncertainties associated with the coarse-graining of the cloud particle properties (i.e., size distribution and shape), subgrid-scale processes, and their complex interactions with radiation, it remains uncertain to what extent these models represent reality.

In this context, studying the well-characterized atmospheres of planets in the Solar System provides invaluable benchmarks. In particular, solar occultation measurements conducted by recent planetary exploration missions offer atmospheric transmission data across different altitudes, which have been conveniently used to construct empirical transit spectra of Solar System planets. For example, the empirical transit spectra of Earth have been reconstructed from the solar occultation data obtained with the Atmospheric Chemistry Experiment Fourier Transform Spectrometer (ACE-FTS) onboard the SCISAT satellite (Schreier et al. 2018; Macdonald & Cowan 2019). Doshi et al. (2022) compared cloud-free and cloudy ACE-FTS/SCISAT data, highlighting the importance of aerosols. They showed that stratospheric clouds increase the transit depth by \sim 10 ppm for an exo-Earth in the TRAPPIST-1 system, which suppresses absorption features of transit

* These authors contributed equally to this work.

spectra. However, this effect does not significantly hinder JWST’s ability to characterize the atmospheres of Earth-like exoplanets.

The role of aerosols has also been explored using Titan as a testbed. [Robinson et al. \(2014\)](#) generated Titan’s transit spectra in the 0.88–5 μm spectral range based on data from the Visual and Infrared Mapping Spectrometer onboard the Cassini spacecraft. Their results demonstrated that high-altitude hazes significantly limit the atmospheric depths that can be probed via transit spectroscopy, restricting observations to pressure levels between 0.1 and 10 mbar. [Changeat et al. \(2025\)](#) analyzed the same transit spectra of Titan using a retrieval framework and found that multiple aerosol components were required to achieve a successful fit.

This study focuses on Mars, which is the second most studied planet in terms of spectroscopic observations, after Earth. Mars has a tenuous atmosphere (6.1 mbar at the surface) with little atmospheric water vapor (\sim 150 ppm) (e.g., [Smith 2008](#)). A distinctive characteristic of Martian atmosphere is the presence of micron-sized airborne dust particles, which significantly influence the planet’s climate by modulating solar radiation and altering the atmospheric thermal structure. Similar to previous works, we aim to obtain empirical transit spectra based on the actual data from ExoMars Trace Gas Orbiter (TGO) mission. While Martian atmospheric structure has been modeled by General Circulation Models (GCMs), which have been extensively validated against observations, GCMs are not necessarily perfect, particularly in their treatment of clouds and hazes. For example, [Stcherbinine et al. \(2022\)](#) compared TGO water-ice cloud vertical profiles with simulations from the Mars Planetary Climate Model (PCM) and found that, while the model reproduces the overall altitude structure, it tends to underestimate cloud-top heights. Our observation-driven approach therefore provides a more direct, model-independent insight. We note that the present atmospheric state of Mars is the outcome of its unique formation and evolutionary history, and thus may not necessarily apply to exoplanets in other systems. However, it serves as a valuable example of a planet residing within the conventional habitable zone while being markedly different from an Earth-like habitable environment. Characterizing the transit spectra of Mars would offer important insights into the observable signatures of dusty and dry worlds.

The organization of this manuscript is as follows: the method for generating empirical transit spectra and the resultant spectra are presented in Section 2. The infrared portion of the spectra, which is most relevant to exoplanet observations, is further analyzed in Sections 3 and 4. In Section 3, we interpret the empirical spectra using forward modeling with an established radiative transfer code, guided by existing knowledge of the Martian atmosphere. Section 4 presents more agnostic retrieval analyses, treating the spectra as if they were obtained from an exoplanet, to evaluate the potential for characterizing Mars-like exoplanets. In Section 5, we further discuss the implications of the two properties of Mars transit spectra, time variability and the 3.1 μm H_2O ice feature, in the context of exoplanet characterization. Finally, Section 6 summarizes the key findings and concludes.

2. EMPIRICAL TRANSIT SPECTRA

2.1. *Dataset and Method for Generating Empirical Transit Spectra*

We reconstruct the empirical transit spectra of Mars using data from the Nadir and Occultation for Mars Discovery (NOMAD) spectrometer onboard ExoMars/TGO, which is specifically designed for solar occultation measurements ([Vandaele et al. 2018](#)). In particular, we utilize data from the Solar Occultation (SO) ([Neefs et al. 2015](#)) and Ultraviolet and VISible spectrometer (UVIS) ([Patel et al. 2017](#)) channels of the NOMAD instrument. As the spacecraft orbits Mars, the Sun as seen by NOMAD moves vertically through

the Martian atmosphere, allowing the instrument to measure transmitted sunlight at different tangential altitudes. The SO channel covers wavelengths of 2–4 μm with a spectral resolving power of $\mathcal{R} = 17,000$ and a spectral resolution of $\Delta\lambda = 0.119\text{--}0.235$ nm, whereas the UVIS channel spans 0.2–0.65 μm with $\mathcal{R} = 100\text{--}500$ and a spectral resolution of $\Delta\lambda = 1.2\text{--}1.6$ nm.

In the SO channel, an Acousto-Optical Tunable Filter (AOTF) serves as a passband filter, selecting specific diffraction orders from the echelle grating, which provides a spectral coverage of approximately 22 cm^{-1} per order. The AOTF allows for instantaneous switching between diffraction orders, and during standard operations, the SO channel typically records five to six orders per measurement. Occasionally, the NOMAD-SO operates in a specialized “full-scan” mode, in which it acquires data across 111 diffraction orders from 2 to 4 μm . In this study, we analyze 29 full-scan observations obtained between 2018 and 2024, covering various locations and seasons on Mars. These observations were selected based on the criterion that full spectra covering 2 to 4 μm were obtained at intervals of at least every 20 km within the 0–100 km altitude range. Figure 1 shows an example of spectra obtained in the full-scan mode of NOMAD/SO. Each diffraction order appears as a region between two adjacent spiky features. These spiky features are likely due to optical modulations occurring during occultation and are subsequently corrected by our data processing routines. As described above, data corresponding to different diffraction orders were acquired at different altitudes (or, equivalently, impact parameters). In this particular spectrum, the data points near 2 μm correspond to an altitude of 19.86 km, while those near 4 μm correspond to an altitude of 22.43 km; the overall increase in transmittance toward longer wavelengths is partly attributed to this variation in altitude. At higher altitudes, the transmittance generally increases because of the reduced air-mass density and optical depth.

In contrast to the SO channel, the UVIS channel continuously covers its entire spectral range using 1024 pixels, though onboard averaging is applied over 8 pixels along the wavelength axis after March 2019. The UVIS channel typically operates alongside the SO channel, and such concurrent measurements are available for 25 out of the 29 full-scan observations. It is important to note that UVIS data are affected by stray light contamination; however, the correction methods developed have been shown to be highly effective at mitigating this issue for wavelengths longer than 220 nm (Willame et al. 2022; Mason et al. 2022). Consequently, data at shorter wavelengths are excluded from our analysis.

In this paper, the empirical transit spectra refer to either the wavelength-dependent transit depth, Δ_λ , or the corresponding wavelength-dependent effective atmospheric thickness, h_λ . The transit depth (Δ_λ) is simply the fractional decrease in stellar flux when a planet passes in front of its host star, often represented in units of parts-per-million (ppm). The effective atmospheric thickness (h_λ), introduced by Kaltenegger & Traub (2009) and often used in presenting modeled transit spectra, represents the wavelength-dependent thickness of an opaque atmosphere which would result in the same transit depth, i.e.,

$$\Delta_\lambda = \frac{(R_p + h_\lambda)^2}{R_\star^2}, \quad (1)$$

where R_p is the planetary radius, and R_\star is the stellar radius. In reality, the atmospheric transmittance gradually changes with the radius (altitude). Denoting the wavelength-dependent transmittance of the optical path with the impact parameter b by $T(b, \lambda)$, transit depth can also be written as

$$\Delta_\lambda = \left(\frac{R_p}{R_\star} \right)^2 + \frac{2}{R_\star^2} \int_{R_p}^{R_\star} b [1 - T(b, \lambda)] db. \quad (2)$$

Combining these two expressions yields

$$h_\lambda = -R_p + \sqrt{R_p^2 + 2 \int_{R_p}^{R_\star} b [1 - T(b, \lambda)] db}. \quad (3)$$

For atmospheres that are much thinner than the planetary radius, as is the case here, this can be approximated by

$$h_\lambda = \frac{1}{R_p} \int_{R_p}^{R_\text{top}} b [1 - T(b, \lambda)] db, \quad (4)$$

where R_top is the radius at the top of the atmosphere. In this study, the transmittance, $T(b, \lambda)$, is derived from the NOMAD observations, and we adopt $R_\text{top} = 100$ km.

The transmittance spectrum as a function of impact parameter, $T(b, \lambda)$, is a key input from the NOMAD measurements. However, it is not trivial to incorporate the NOMAD data into $T(b, \lambda)$, because the actual NOMAD measurements constitute a non-systematic collection of fragmented data, each taken within a narrow wavelength range (in the case of the SO channel), at a specific altitude, and at a specific location on the planet. The raw data are also affected by a signal bias due to the AOTF, which is particularly prominent near the edges of individual diffraction orders (Figure 1). To construct representative empirical transit spectra from these measurements, the following procedures are applied:

1. Average the transmittance spectra over each spectral interval to minimize the bias (applicable only to SO channel data);
2. Interpolate the transmittance profiles along altitude to achieve regular vertical sampling (for SO channel data, this step is performed separately for each spectral interval);
3. Compute the h_λ spectrum at each observed latitude using Equation 4, based on the interpolated transmittance profiles;
4. Classify the set of h_λ based on Martian season and latitude;
5. Average the calculated h_λ spectra over latitude for each Martian season.

In Step 1, the bias observed in the SO channel data is corrected. As shown in Figure 1, the spectrum of a given diffraction order displays a curved continuum, likely due to optical modulation. Among the 320 data points in each order, the first and last 100 pixels exhibit significant curvature. To minimize their impact, we use only the central 120 pixels of each spectrum (highlighted in red in Figure 1) and compute the mean transmittance. This processing results in spectra with relatively low spectral resolution ($\mathcal{R} \sim 140$) where each data point is associated with an altitude (or impact parameter). Note that gaps are present between diffraction orders in the spectral coverage, which may introduce errors when comparing with radiative transfer simulations that assume continuous spectral data.

The second step (Step 2) is to obtain the transmittance spectrum as a function of altitude. For a given wavelength range, transmittance values as a function of impact parameter are linearly interpolated along altitude at 1 km intervals, spanning from 0 to 100 km. Figures 2a, 2b present an example of the resulting NOMAD/SO transmittance as a function of altitude. In panel 2a, the dotted curves represent spectra averaged over each diffraction order, while the solid lines indicate the interpolation. Panel 2b displays the transmittance at different altitudes and wavelengths by the color gradients. This highlights that the lower

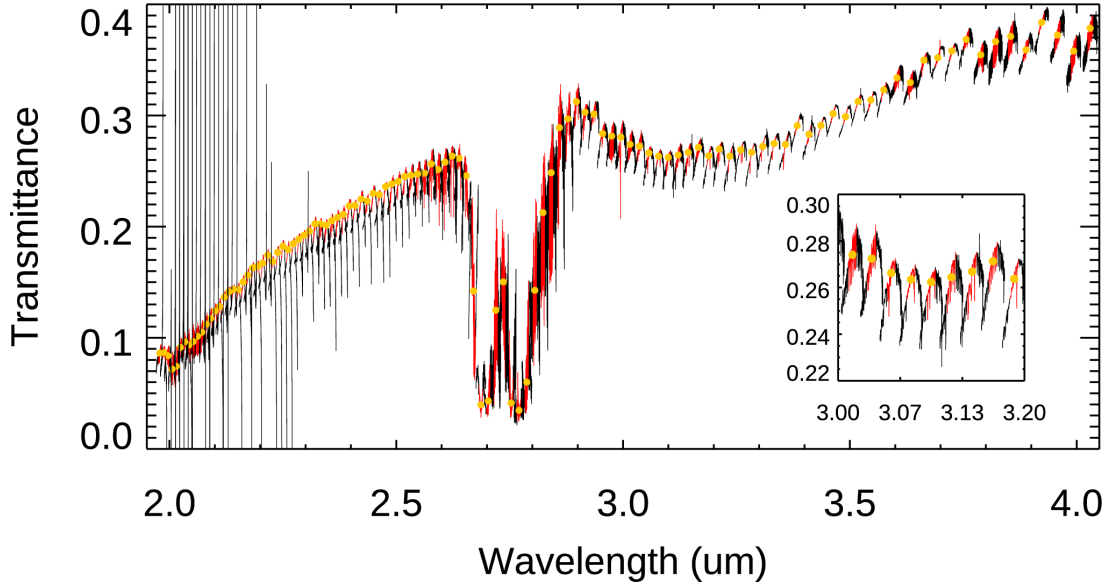


Figure 1. An example of spectra obtained by NOMAD/SO in full-scan mode. The spectra were taken between 19.86 km and 22.43 km above the surface of Mars. The red curves indicate the central 120 pixels of each spectrum, which are averaged to produce empirical spectra with low spectral resolution. The averaged transmittances for each diffraction order are shown as orange dots. The inset at the lower right shows a zoomed-in view of the 3.0–3.2 μm region.

atmosphere appears opaque due to the presence of aerosols and molecular absorption. Similar to the SO channel data reduction, the UVIS data are also interpolated along the altitude. Figures 2c, 2d present an example of the NOMAD/UVIS spectrum.

The third step (Step 3) is to compute the effective height using Equation 1.

Following this, Step 4 involves classifying the dataset based on Martian season and latitude. It is important to note that Mars experiences seasons, similar to Earth, considering that both planets have a similar obliquity. As illustrated in Figure 3, Solar longitude (Ls) values of 0° and 180° correspond to the northern spring and autumn equinoxes, respectively, while Ls values of 90° and 270° correspond to the northern and southern summers, respectively. During the northern summer, the distance between the Sun and Mars is relatively large, resulting in lower atmospheric temperatures. This leads to a higher abundance of H_2O ice clouds in the upper troposphere and a lower presence of dust (e.g., Smith 2008). Therefore, this season is sometimes referred to as the “non-dusty period”. In contrast, the southern summer is known as the “dusty period,” as the Sun is closer to Mars, leading to higher atmospheric temperatures and increased dust levels (e.g., Smith 2008). To take account of the possible seasonal variations, we classified the transmittance data into the following three periods and reconstructed the transit spectrum separately: the northern summer period ($\text{Ls} = 30\text{--}150^\circ$), the southern summer period ($\text{Ls} = 210\text{--}340^\circ$), and the equinox period ($\text{Ls} = 340\text{--}30, 150\text{--}210^\circ$). Figure 4 displays the calculated effective heights, with the spectra shown separately for the three seasons. In this figure, the spectra are shown for the northern summer period ($\text{Ls} = 30\text{--}150^\circ$) in panel (a), the southern summer period ($\text{Ls} = 210\text{--}340^\circ$) in panel (b), and the equinox period ($\text{Ls} = 340\text{--}30, 150\text{--}210^\circ$) in panel (c). The color variations in each panel represent the latitudes of the measurements. This demonstrates that the spectral shape exhibits significant variability depending on latitude, even within the same seasonal period, largely reflecting latitudinal differences in dust and water-ice cloud loading.

The final step of the procedure, Step 5, involves averaging the effective height spectra over latitude to construct representative empirical transit spectra. Each effective height spectrum at a given latitude, h_λ , is

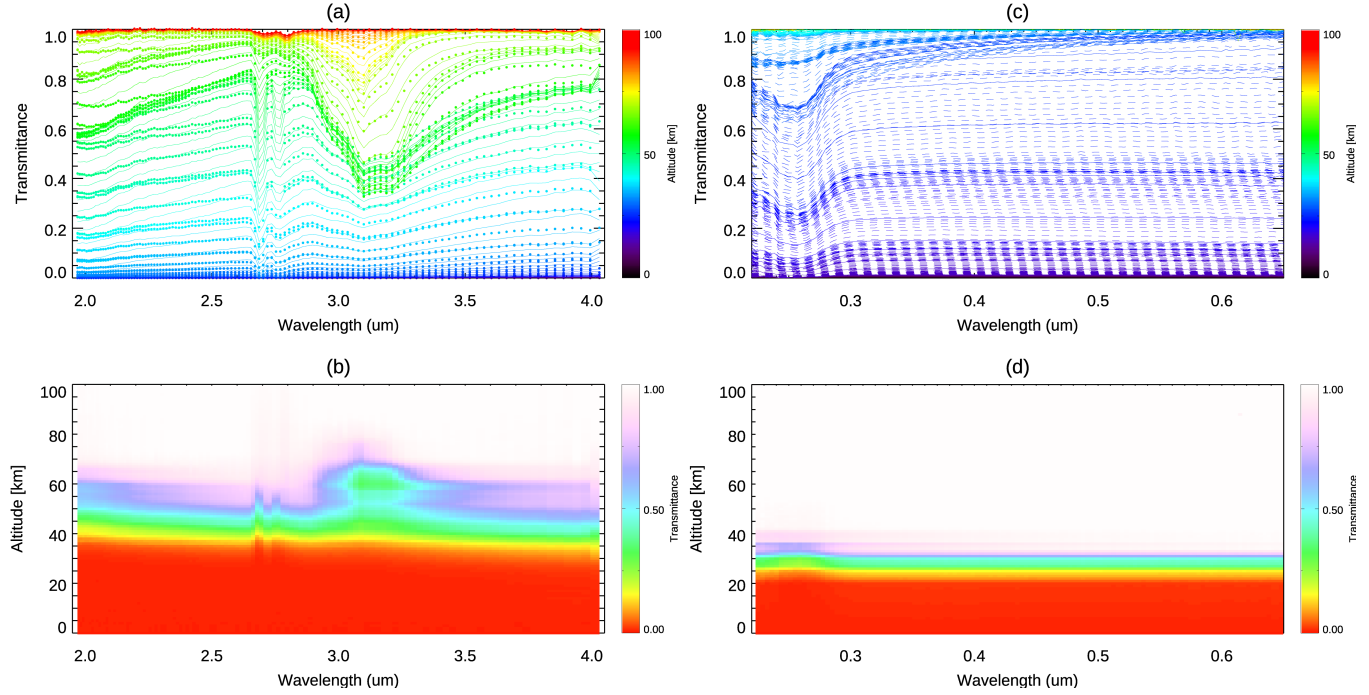


Figure 2. (a,b) An example of the transmittance spectra taken with the full-scan mode of the SO channel of TGO/NOMAD. (c,d) An example of the transmittance spectra taken with the full-scan mode of the UVIS channel.

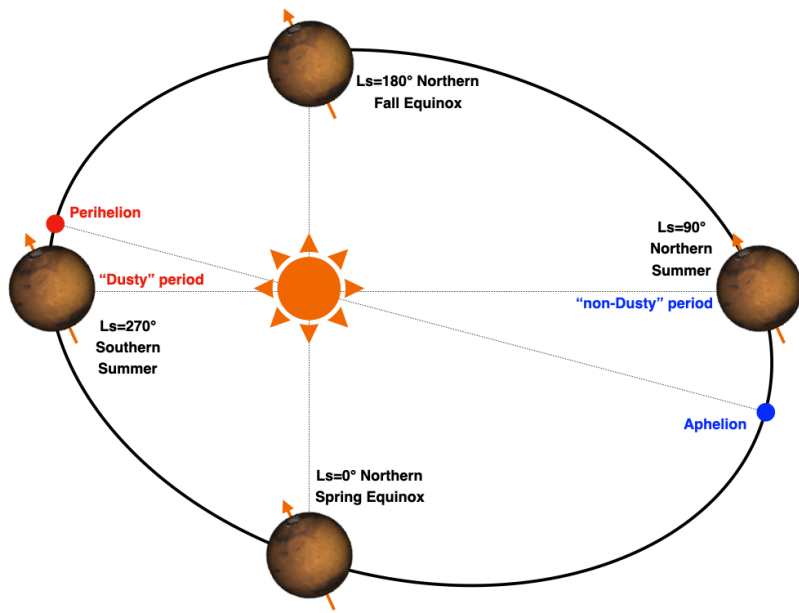


Figure 3. Illustration of the relationship between the Sun and Mars throughout a Martian year. The solar longitude (L_s) is the angle between the Sun and Mars, measured from the position of the Northern hemisphere's spring equinox, defined as $L_s = 0^\circ$. Thus, $L_s = 90^\circ$ corresponds to the northern summer solstice, $L_s = 180^\circ$ marks the northern autumn equinox, and $L_s = 270^\circ$ corresponds to the northern winter solstice.

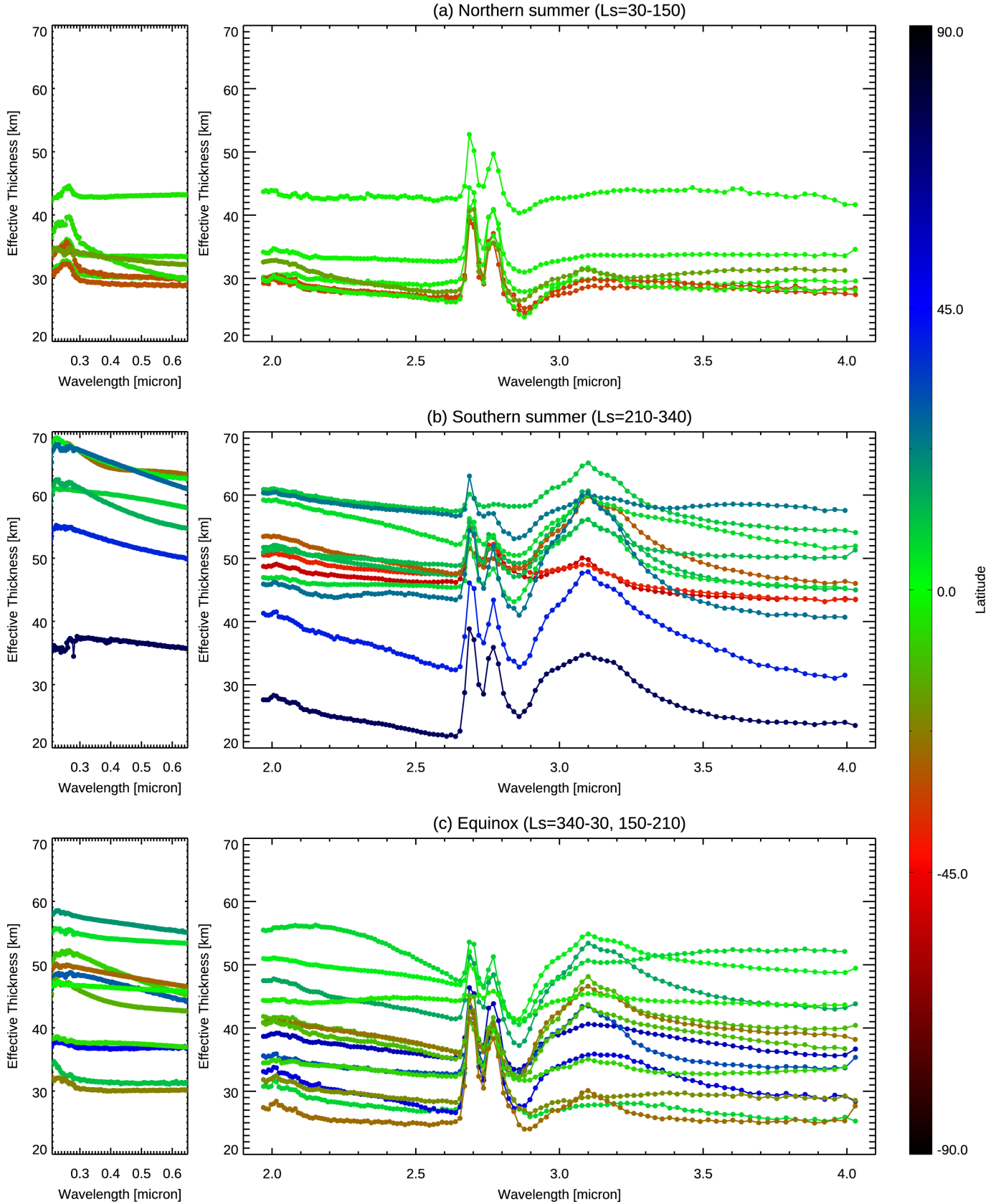


Figure 4. Empirical transit spectra generated from the TGO/NOMAD Solar occultation measurements taken at (a) northern summer ($L_s=30-150^\circ$), (b) southern summer ($L_s=210-340^\circ$), and (c) equinox ($L_s=340-30^\circ, 150-210^\circ$). The color variation represents the latitudes of the measurements. The results obtained from the UVIS and infrared SO channels are shown in the left and right panels, respectively.

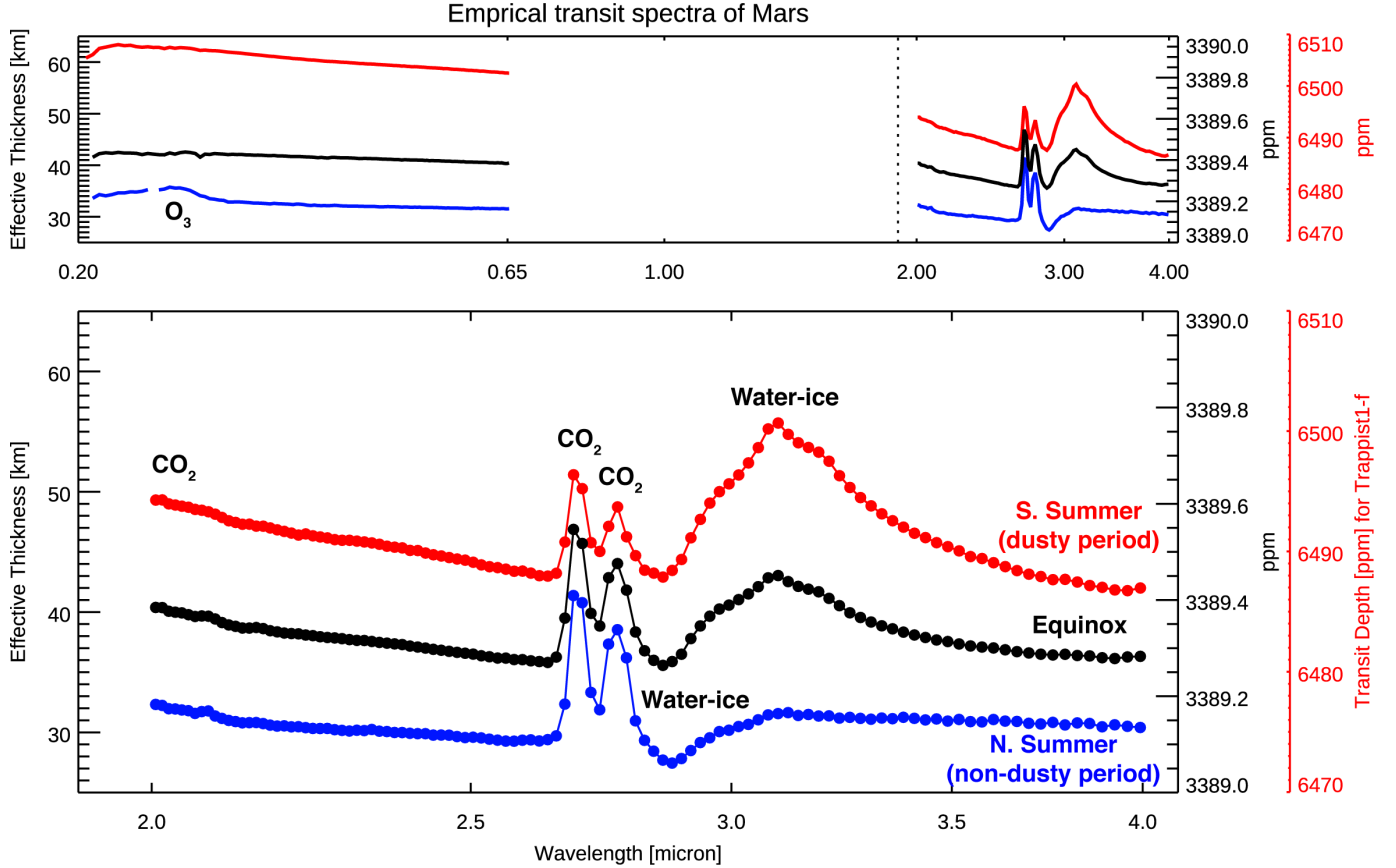


Figure 5. Empirical transit spectra of Mars derived from TGO/NOMAD measurements are shown for the northern summer period (blue curve), equinox period (black curve), and southern summer period (red curve). The right y-axis indicates the transit depth for Mars (black axis), scaled to represent the case of TRAPPIST-1f.

first grouped into latitude bins spanning from -90° to $+90^\circ$ in 30° increments. The spectra within each bin are then averaged, and finally, a global mean spectrum is obtained by averaging across all latitude bins.

2.2. Spectral Features in the Generated Empirical Transit Spectra

Figure 5 presents representative empirical transit spectra, averaged separately over the three different periods shown in Figure 4. As illustrated, the effective thickness of Mars' transit spectra ranges between 25 and 65 km, indicating that the atmosphere below ~ 25 km (~ 0.5 mbar) is largely opaque. The effective thickness varies with the Martian season, being greater during dusty periods and smaller during non-dusty periods. We note that using the NOMAD/SO spectra without averaging over the diffraction order yields a consistent baseline effective thickness (not shown), indicating that the atmosphere remains opaque below 25 km due to aerosol opacity even when the spectral resolution is increased.

Figure 5 highlights two distinct spectral features: CO_2 absorption at $2.7\text{--}2.8\ \mu\text{m}$ and H_2O ice cloud signatures near $3\ \mu\text{m}$, along with the continuum slope. The amplitude of the CO_2 absorption features corresponds to an effective thickness of approximately 10 km, varying with Martian seasons. This absorption is slightly weaker at dusty period. Weak features at $2.0\text{--}2.1\ \mu\text{m}$ are also due to CO_2 .

The prominent H_2O ice cloud feature is intriguing given the low abundance of water in Mars' atmosphere and the limited attention such clouds have received in previous studies. The feature is more prominent in

the warmest “Southern summer” season, which may be counterintuitive given that the mesospheric clouds would form in a cold environment. We will further study this seasonality in Section 3.

In the UV, a weak O₃ feature appears near 0.25 μm , and is more pronounced during Northern summer (the non-dusty season). This variation reflects the well-known seasonal cycle of Martian ozone. O₃ is produced from CO₂ photolysis and is efficiently destroyed by hydrogen radicals originating from water vapor (e.g., Lefèvre et al. 2021). During the non-dusty season, water vapor is largely confined to the lower atmosphere (below \sim 15 km) (e.g., Aoki et al. 2022), which reduces HO_x-driven ozone loss and leads to higher ozone abundances (e.g., Patel et al. 2021).

In both wavelength domains, the transit spectra exhibit a spectral slope, with the effective thickness increasing toward shorter (UV) wavelengths. The spectral slope can be quantified using the power-law index of opacity, α , defined by $\kappa \propto \lambda^\alpha$, which is related to the effective height through $H\alpha = \frac{d\text{height}}{d\log\lambda}$ (e.g., Lecavelier Des Etangs et al. 2008). In the 2–2.6 μm range, the observed slope corresponds to $\alpha \sim -2$. This is shallower than the Rayleigh expectation, indicating that aerosols dominate the continuum opacity in this spectral region. On the UV, the spectral index is smaller than this. If the infrared and UV slopes share a common origin, the change in the spectral gradient between 0.65 and 2 μm suggests characteristic aerosol particle sizes of order $\sim 1 \mu\text{m}$. We note, however, that the two slopes may not necessarily be explained by a single aerosol population. Analyses combining UV and IR solar occultation data suggest that a bimodal aerosol size distribution may be required (Fedorova et al. 2014). Investigating such UV-specific complexity is beyond the scope of the present work.

3. INTERPRETATION WITH INFORMED FORWARD MODELING

In this section, the derived empirical transit spectra are quantitatively interpreted through comparisons with modeled spectra (i.e., forward modeling). We focus on the infrared portion of the spectra, motivated by its relevance to potential exoplanet applications. This choice is driven not only by the success of infrared spectroscopy with JWST in characterizing atmospheric compositions, but also by the fact that promising targets for transit spectroscopy among potentially habitable planets are typically orbiting low-mass stars, which are intrinsically faint in the ultraviolet and visible wavelengths and thus subject to high photon noise in those bands. We generated synthetic spectra using the Planetary Spectrum Generator (PSG) (Villanueva et al. 2018), a radiative transfer suite widely used for analyzing spectroscopic observations of Mars, including those from TGO/NOMAD (e.g., Villanueva et al. 2021) and those from ground-based observations (e.g., Aoki et al. 2024), as well as for other Solar System bodies and exoplanets.

3.1. *Inputs for Forward Modeling with PSG*

To compute synthetic transit spectra of Mars, we simulate observations of Mars transiting the Sun from a distance of 10 parsecs to fully emulate the geometry of a Mars transit event although the exact distance does not affect the noise-free spectra. PSG performs radiative transfer calculations using the line-by-line method for high spectral resolution and the correlated-k method for low spectral resolution, and we employed the latter for interpreting these spectra. The instrumental line shape was modeled as a Gaussian with a spectral resolving power (\mathcal{R}) of 140. This value reflects the averaging of the original NOMAD spectra—initially at $\mathcal{R} \sim 17,000$ —across more than 120 spectral points.

For our PSG simulations, we employ the default Martian atmospheric settings, which provide a vertical resolution of approximately 5 km in the 20–80 km altitude range. The calculations include molecular absorptions from CO₂, H₂O, and CO, as well as extinction due to dust and H₂O ice clouds, and Rayleigh scattering. Molecular absorption coefficients were taken from the HITRAN2020 database (Gordon et al.

2022), using CO₂ pressure-broadening coefficients. Dust extinction coefficients were based on Wolff et al. (2009), using CRISM data from MRO, while H₂O ice cloud extinction coefficients were derived from Warren & Brandt (2008).

The temperature structure at each season, as well as the molecular profiles, were fixed to the values predicted by the Martian Climate Database (MCD, Millour et al. 2018) at those instances as implemented in PSG. We further assume the basic properties of the dust and H₂O ice clouds. Namely, the representative vertical extent and particle size of the aerosols were defined a priori based on the knowledge about Mars as described below. However, their mixing ratios and the particle size of H₂O ice clouds were tuned to fit the data within the range of observed values. Specifically, the volume mixing ratios were varied between 0.1 and 50 ppm for both dust and H₂O ice clouds, while the effective particle size of H₂O ice clouds was adjusted within the range of 0.1 to 10 μm (Liuzzi et al. 2024).

For dust, the effective particle size is fixed at 1.5 μm , and their vertical distribution is assumed to be uniform. We note that, in reality, occasional non-well-mixed vertical profiles, such as detached layers, have been suggested (e.g., Heavens et al. 2011).

For H₂O ice clouds, we consider two types: low-altitude clouds in the upper troposphere (10–40 km) and high-altitude clouds in the mesosphere (40–70 km). The volume mixing ratio and effective particle size of the H₂O ice clouds in each layer are adjusted accordingly. This is based on the known properties of Martian clouds. In the Martian upper troposphere, one of the most prominent occurrences of H₂O ice clouds is the so-called “equatorial cloud belt,” which forms in specific low-latitude regions. This cloud belt develops as air cools in the ascending branch of the Hadley circulation during the northern spring–summer season, when atmospheric temperatures are relatively low due to Mars’ greater distance from the Sun (e.g., Montmessin et al. 2004). The particle sizes of these stratospheric H₂O ice clouds are typically on the order of a few microns. On the other hand, mesospheric H₂O ice clouds had been identified relatively recently (e.g., Clancy et al. 2019), and have been systematically studied using the datasets same as what we use here, based on solar occultation measurements by TGO (e.g., Liuzzi et al. 2020, 2024; Stolzenbach et al. 2023a,b). These studies revealed that sub-micron-sized H₂O ice clouds are widely present in the mesosphere during the southern spring–summer season, when water vapor directly reaches mesospheric altitudes (e.g., Aoki et al. 2022). To take account of such known size difference between the stratospheric cloud and mesospheric clouds, we treat these two clouds separately, with the division at 40 km altitude.

3.2. Comparison Between Empirical Transit Spectra and Forward Model Results

Figure 6 compares the empirical and synthetic transit spectra, with the assumed vertical profiles shown in the right panel. This figure demonstrates that simple forward modeling, based on a single representative atmospheric structure, can effectively reproduce the observed empirical transit spectra.

The seasonal variation in CO₂ absorption at 2.7–2.8 μm is successfully reproduced by the PSG simulations. The depth of the feature appears slightly weaker during periods of higher atmospheric dust loading. Since CO₂ is the dominant component of the Martian atmosphere, maintaining an almost constant volume mixing ratio of 99.6 percent throughout the year, these seasonal changes in CO₂ absorption are not due to changes in gas abundance. Instead, they are attributed to the influence of aerosols—primarily dust particles—whose mixing ratio varies in season. These aerosols add to the total opacity of the atmosphere, thereby increasing the peak effective thickness at the CO₂ absorption band. In addition, they diminish the spectral signatures of CO and H₂O. Although the absorption features of H₂O and CO are centered at 2.6 μm and 2.35 μm , respectively (see green and light blue curves in Figure 6), these features are largely masked in the empirical transit spectra due to aerosol opacity. Theoretically, the spectral features of CO and H₂O

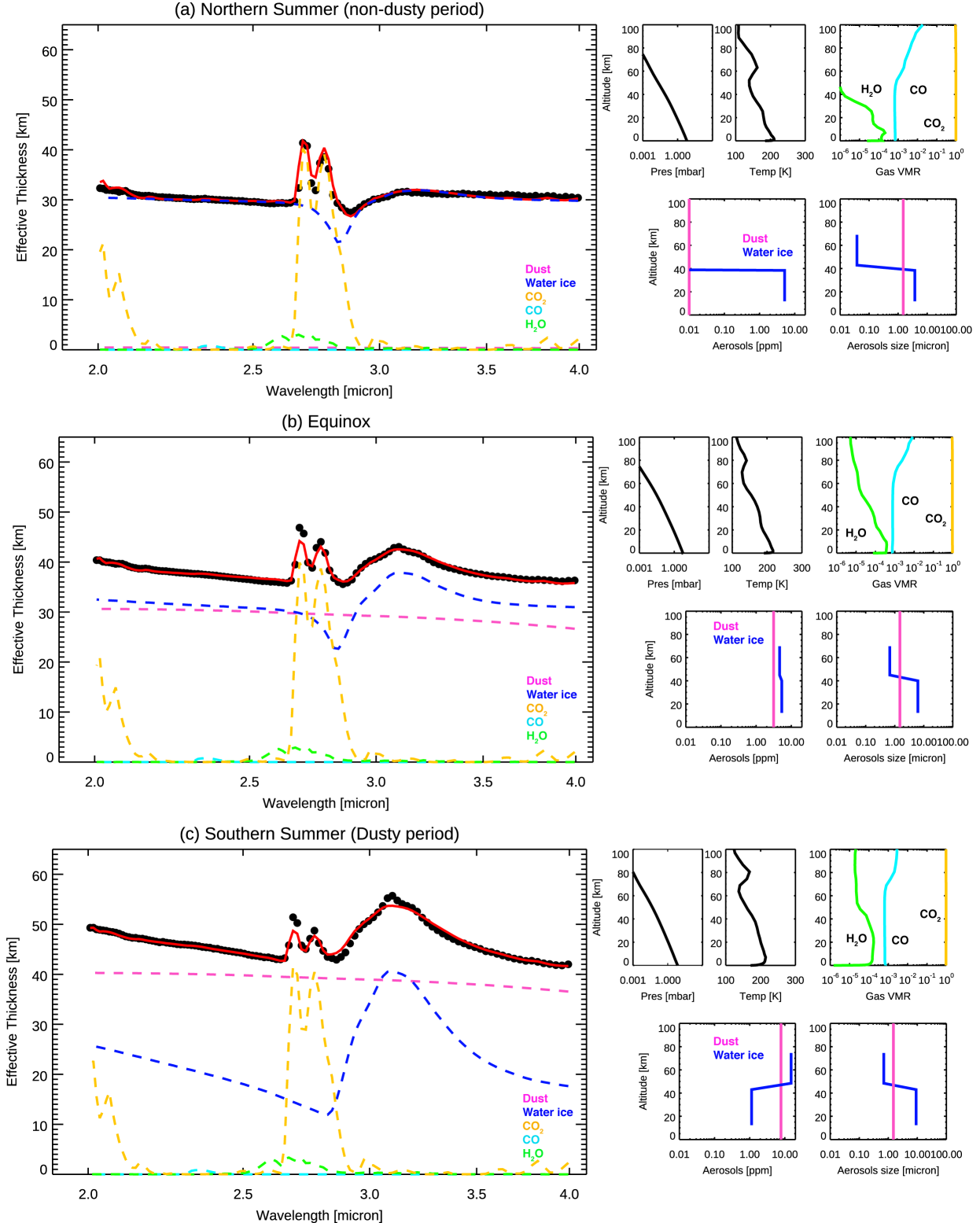


Figure 6. A comparison between the empirical transit spectra of Mars, derived from TGO/NOMAD solar occultation measurements, and synthetic spectra calculated using PSG—based on a single representative atmospheric structure—is presented in the left panels for the northern summer period (a), equinox period (b), and southern summer period (c). The black curves represent the empirical transit spectra, the red curves correspond to the PSG synthetic spectra, and the other colors indicate the individual spectral contributions. The right panels show the assumed vertical profiles of pressure, temperature, gas mixing ratios (H_2O , CO , CO_2), aerosol properties (dust and H_2O ice clouds), and aerosol particle sizes.

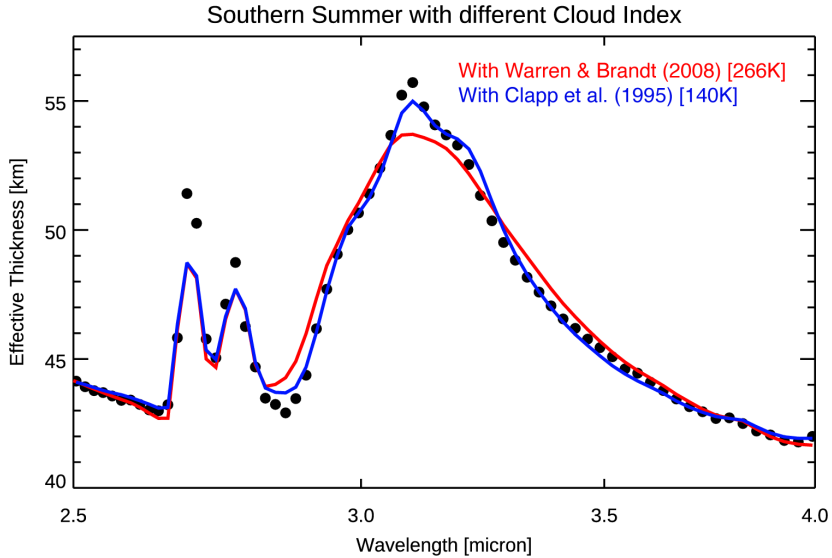


Figure 7. Same as the left panel in Fig. 6c but comparison between the synthetic spectra calculated with refractive index of H_2O ice clouds by Clapp et al. (1995) (blue) and Warren & Brandt (2008) (red).

become more discernible at higher spectral resolving power—for example, corresponding to an effective thickness variation of 1 km at a resolution of $R = 5000$ —even in the presence of dust and water ice clouds (not shown). This underscores the critical role of dust in shaping the vertical sensitivity of transit spectra and highlights the strong seasonal variability of spectral features as a defining characteristic of Mars’ dusty atmosphere.

The PSG simulation also successfully captures the seasonal variability of H_2O ice cloud signatures near $3 \mu\text{m}$. The reduced effective thickness around $2.9 \mu\text{m}$ in the northern summer transit spectra (Fig. 6a) is attributed to the presence of larger H_2O ice particles, with radii exceeding $1 \mu\text{m}$. In contrast, the enhanced effective thickness around $3.1 \mu\text{m}$ in the equinox and southern summer transit spectra (Figs. 6b, c) is attributed to the small H_2O ice particles with sizes smaller than $1 \mu\text{m}$, consistent with the sub-micron-sized mesospheric clouds on Mars. Indeed, the presence of sharp $3.1 \mu\text{m}$ feature requires the presence of sub-micron-sized particles, as we will discuss later (e.g., Figure 9 below). We note that the sharp peak of the H_2O ice cloud feature at $3.1 \mu\text{m}$ is not perfectly reproduced by the forward simulation (see Figure 6c). This discrepancy likely arises from the temperature dependence of the optical constants of H_2O ice. The assumed refractive index of H_2O ice from Warren & Brandt (2008) is based on laboratory measurements at 266 K, which is higher than the actual temperature of the Martian mesosphere (approximately 140 K). A forward simulation using the refractive index measured at 140 K by Clapp et al. (1995) provides a better match at the $3.1 \mu\text{m}$ peak (Figure 7). However, that refractive index dataset is not used in other parts of this study due to its limited spectral coverage, only longer than $2.5 \mu\text{m}$.

4. POTENTIAL OF CHARACTERIZING MARS-LIKE EXOPLANETS

In this section, we aim to quantify the detectability of the characteristic features seen in Mars’ transit spectra assuming it were observed as an exoplanet. To this end, we consider a scenario in which one of the known transiting exoplanets orbiting nearby low-mass stars, TRAPPIST-1f, has an atmospheric T - P profile similar to that of Mars. TRAPPIST-1f is one of the “golden” targets for atmospheric characterization among temperate Earth-sized exoplanets. It receives an insolation comparable to what Mars receives from the Sun, making it an ideal testbed for our study. We generate mock data by adding artificial noise to the empirical

transit spectra introduced in Section 2, and analyze it using a retrieval framework commonly employed in the study of exoplanet spectroscopy. As in previous section, we focus exclusively on the infrared portion of the spectra, as it is most relevant to foreseeable exoplanet observations (see Section 3). The procedure is detailed in Section 4.1 and the result is presented in Section 4.2.

The reason for not assuming a Mars-twin around solar-type stars is not only that such planets have not been discovered in the solar neighborhood but also that the atmospheric signals of a Mars-twin orbiting a Sun-like star are as low as 0.1 ppm of the stellar light (e.g., Fujii et al. 2018), which is too small to be detectable under statistic and systematic noises. Nevertheless, the estimate for the required precision provided below can be trivially scaled to such cases when needed.

4.1. Method: Preparation of input data and analysis framework

4.1.1. Input data

We scale the empirical transit spectra of Mars to TRAPPIST-1f as follows. First, the effective thickness is scaled according to the scale height. Specifically,

$$h_{\text{T1f}} = h_{\text{Mars}} \frac{H_{\text{T1f}}}{H_{\text{Mars}}} = h_{\text{Mars}} \frac{g_{\text{Mars}}}{g_{\text{T1f}}} \frac{T_{\text{T1f}}}{T_{\text{Mars}}} = h_{\text{Mars}} \frac{M_{\text{Mars}}}{M_{\text{T1f}}} \left(\frac{R_{\text{T1f}}}{R_{\text{Mars}}} \right)^2 \left(\frac{S_{\text{T1f}}}{S_{\text{Mars}}} \right)^{1/4} \sim 0.4h_{\text{Mars}}, \quad (5)$$

where H_X , g_X , M_X , R_X , T_X , and S_X are the scale height, surface gravity, mass, radius, equilibrium temperature, and incident flux, respectively, of planet X . To obtain the right-hand side, we used the astrophysical parameters of TRAPPIST-1 as the host star and TRAPPIST-1f as the planet given by Agol et al. (2021), specifically $M_{\text{T1f}} = 1.039M_{\oplus}$, $R_{\text{T1f}} = 1.045R_{\oplus}$, and $S_{\text{T1f}} = 0.373S_{\oplus}$ combined with $M_{\text{Mars}} = 0.107M_{\oplus}$, $R_{\text{Mars}} = 0.53R_{\oplus}$, and $S_{\text{T1f}} = 0.43S_{\oplus}$. The transit depth is then calculated as $(R_{\text{T1f}} + h_{\text{T1f}})^2/R_{\text{T1}}^2$ ($\sim (R_{\text{T1f}}/R_{\text{T1}})^2 + 2R_{\text{T1f}}h_{\text{T1f}}/R_{\text{T1}}$). This scaling is presented on the y2-axis of Figure 5.

We simply impose noise levels of 3 ppm, 5 ppm, and 10 ppm per wavelength bin on the scaled signal and use the resulting data as mock observations for retrieval analysis. The JWST Exposure Time Calculator (ETC) estimates that a 1-hour exposure (corresponding ~ 1 transit) at $\lambda \sim 3\mu\text{m}$ with the NIRSpec Prism/CLEAR configuration yields a signal-to-noise ratio of $\sim 9,700$ with respect to the stellar flux, for spectral elements with a width of $\Delta\lambda = 0.013\mu\text{m}$. This is equivalent to ~ 100 ppm noise. Given that the noise inversely scales with the square root of the photon counts, and therefore with the square root of the wavelength-bin width, this 100-ppm noise corresponds to ~ 81 ppm noise for the spectral-element width of our data, $\Delta\lambda \sim 0.0212\mu\text{m}$ at $\sim 3\mu\text{m}$. By accumulating photon counts, the noise decreases to ~ 10 ppm in 65 hours, to 5 ppm in ~ 260 hours, or to 3 ppm in ~ 720 hours. The latter two are probably too long to be practical, and achieving such precisions would likely be hindered by the presence of systematic noise. Thus, these cases illustrate the potential capabilities of future observatories beyond JWST.

4.1.2. Retrieval framework

For the retrieval analysis, we used `petitRADTRANS` (Mollière et al. 2019), a frequently used open-source code for analyzing exoplanet atmospheric data. While Section 3 takes account of the detailed vertical atmospheric structures, such complexities are unlikely to be constrained from low-spectral-resolution, low-SNR spectra without any prior knowledge of the surface environment of the planet. Thus, this section simply assumes a 1-dimensional atmospheric profile with constant mixing ratios of molecules and condensates, in a similar manner to the standard analysis of exoplanet data.

For the atmospheric opacity, we considered CO₂, H₂O ice, and an agnostic power-law slope. From the standpoint of being more agnostic or blind, we also searched for other typical molecules that could potentially explain the spectral features and thus be misidentified, but did not find any. Although the 3.0 μm NH₃ band and the 3.3 μm CH₄ band partially overlap with the 3.1 μm feature, our retrievals confirm that the differences in the peak wavelengths prevent misidentification. Including either species does not improve the fit significance. Therefore, we do not consider these additional species further.

We employ the default k -table for the opacity of CO₂ based on the ExoMol line database (Yurchenko et al. 2020), where the line profiles are collision-broadened by H₂. We used the opacity table for H₂O ice with varying particle size provided by `petitRADTRANS` based on Smith et al. (1994). The ice particles are assumed to be spheres where the opacity is calculated using the Mie theory, and the possible effects of irregular or fractal shapes of ice particles are not taken into account. The particle size distribution is assumed to be a log-normal function represented by the average size (effective size; r_{eff}) and the standard deviation (σ_r), which are set as fitting parameters. The power-law continuum opacity is characterized by the opacity at a reference wavelength of 0.35 μm , κ_s , and the power-law index, s , such that $\kappa(\lambda) = \kappa_s(\lambda/0.35\,\mu\text{m})^s$. The parameters for retrieval, as well as their prior distributions, are summarized in Table 1.

Table 1. Fitting parameters for retrievals and their priors

Symbol	Description	Range of flat prior
R_p	Radius [R_\oplus]	[0.993, 1.10] ([0.95-1.05] \times (fiducial))
T	Temperature [K]	[100, 300]
$\log \kappa_s$	\log_{10} (continuum opacity [$\text{cm}^2 \text{ g}^{-1}$] at 0.35 μm)	[-2, 0]
s	power-law index for continuum opacity	[-3, 0]
$\log x_{\text{CO}_2}$	\log_{10} (CO ₂ mass mixing ratio)	[-16, 0]
$\log \mu_{\text{H}_2\text{O}}$	\log_{10} (H ₂ O(s) mass mixing ratio)	[-16, 0]
$\log r_{\text{eff}}$	\log_{10} (effective radius of H ₂ O(s))	[-8, -2]
$\log \sigma_r$	standard deviation of H ₂ O(s) particle radius	[0.04, 3.0]

4.2. Retrieval results

The retrieval results for the empirical transit spectrum during the equinox period on Mars, assuming noise levels of 3 ppm and 5 ppm, are presented in Figure 8. The case with 10 ppm noise is unconstrained (not shown). The posterior distribution indicates that the presence of CO₂ and H₂O ice is inferred at a noise level of 3 ppm, with a flat continuum ($s \sim 0$). To quantify the significance of the CO₂ and H₂O ice detections, we performed additional retrievals without CO₂ and/or H₂O ice, and compared the Bayesian evidences, with variations in the noise realization. The Bayes factor comparing the CO₂+continuum model to the continuum-only model is $> 10^2$, while that comparing the full model (CO₂+H₂O+continuum) to the CO₂+continuum model is also $> 10^2$. These results indicate a “decisive” preference for the full model, according to Jeffreys’ scale (Jeffreys 1939).

The effective radius of H₂O ice, as well as the width of the size distribution, is well-constrained at a noise level of 3 ppm. Specifically, the particle size larger than 1 μm is strongly disfavored. The upper limit arises from the known fact that the 3 μm feature is substantially suppressed at $r_{\text{eff}} \gtrsim 1 \mu\text{m}$. This behavior is

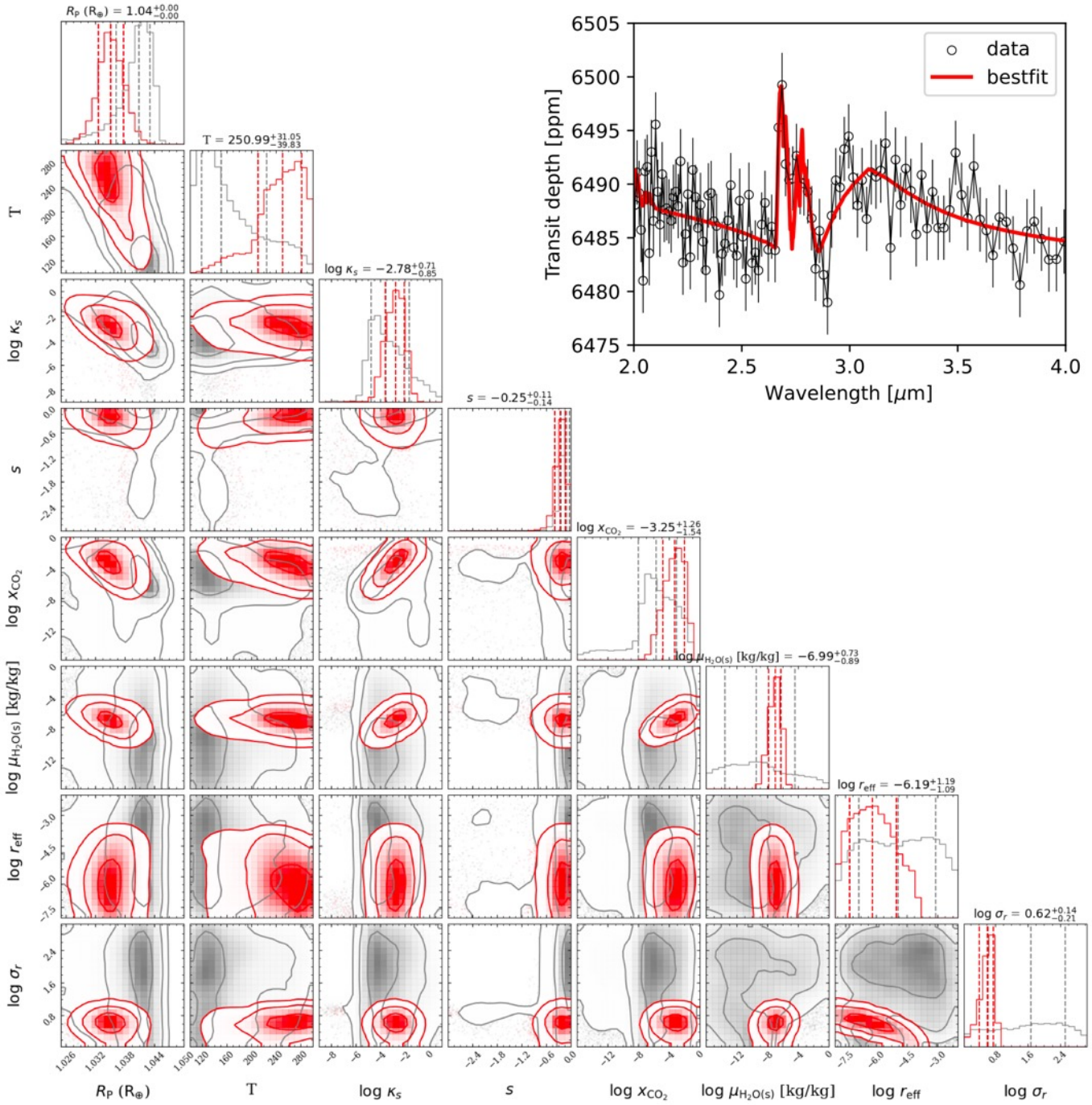


Figure 8. (Left) Corner plot of the retrieval results with varying noise: 3 ppm (red) and 5 ppm (gray). (Upper right): Best-fit spectrum fitted to the data with 3 ppm noise.

illustrated in Figure 9, which shows the dependence of the transit spectrum on the particle size of H_2O ice cloud. In general, the absorption feature appears only in the Rayleigh regime, where $2\pi r_{\text{eff}}/\lambda < 1$.

The number density of H_2O ice cloud particles at the transit radius at $\lambda = 3.1 \mu\text{m}$, denoted by n_0 , can be estimated from the condition that the slant optical depth is order of unity. Letting κ_{ice} represent the mass

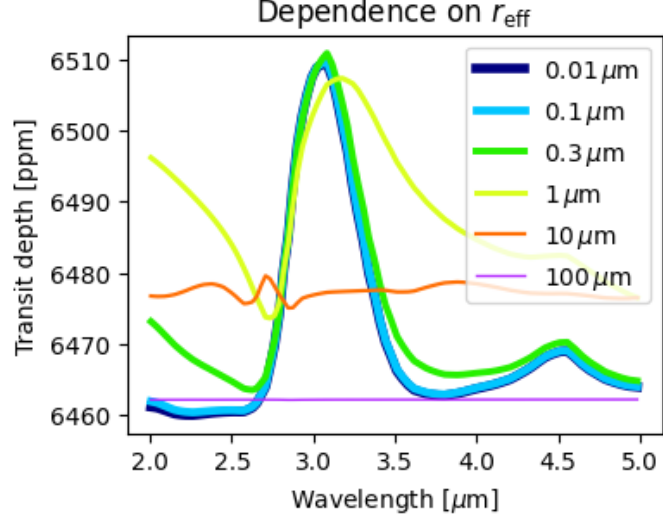


Figure 9. Dependence of the $3.1\text{ }\mu\text{m}$ H_2O ice feature on the effective radius of H_2O ice clouds. The CO_2 feature and slope is removed. The standard deviation of the radius distribution, assumed to be log-normal, is assumed to be $\ln(\sigma_r) = 0.1$. Planetary parameters are set to the values of TRAPPIST-1f.

extinction coefficient of H_2O ice, this condition can be expressed as (e.g., Fortney 2005)

$$\kappa_{\text{ice}} \frac{4\pi r^3 \rho_{\text{ice}} n_0}{3} \sqrt{2\pi R_p H} \left(\sim \tau_{\text{ice, nadir}} \sqrt{\frac{2\pi R_p}{H}} \right) \sim 1, \quad (6)$$

where ρ_{ice} and r are the density and radius of H_2O ice cloud particles, while $\tau_{\text{ice, nadir}}$ represents the vertical optical depth. Substituting representative values of $\kappa_{\text{ice}} \sim 10^4 \text{ cm}^2 \text{ g}^{-1}$ at $3.1\text{ }\mu\text{m}$, $\rho_{\text{ice}} \sim 10^3 \text{ kg m}^{-3}$, $R_p \sim R_{\oplus}$, and $H \sim 10^4 \text{ m}$ yields

$$n_0 \sim 10^9 \left(\frac{r}{0.1\text{ }\mu\text{m}} \right)^{-3} [\text{m}^{-3}] \quad (7)$$

However, the mass *mixing ratio* of H_2O ice clouds remains unconstrained. This is because the pressure level (or equivalently, the density of the ambient atmosphere) at which the absorption bands originate is not well determined. This represents the known degeneracy between the reference pressure level and the molecular mixing ratios (e.g., Benneke & Seager 2012; Heng & Kitzmann 2017). Specifically, a small mixing ratio at high pressure and a large mixing ratio at low pressure can yield a similar number density n_0 , and thus produce comparable absorption depths.

Similarly, the mixing ratio of CO_2 is unconstrained, and the solution with 100% CO_2 is not particularly favored. Meanwhile, the *relative* abundances of multiple species are constrained by the relative strengths of their spectral features. The posterior distribution of x_{CO_2} and $X_{\text{H}_2\text{O}}$ (Figure 8) suggests a dependence of $x_{\text{CO}_2} \sim (X_{\text{H}_2\text{O, (s)}}/10^{-5.5})^2$. The power-law index of 2 likely reflects the scaling of collisionally broadened CO_2 opacity, which is proportional to $n_{\text{CO}_2} p \propto x_{\text{CO}_2} p^2$, where n_i is the number density of species i and p is the atmospheric pressure. In contrast, the H_2O ice opacity scales as $n_{\text{H}_2\text{O}} \propto X_{\text{H}_2\text{O}} p$. Maintaining a constant ratio of these opacities across varying reference pressure levels leads to the above relation. Note that the upper limit of x_{CO_2} is unity, and correspondingly, the upper limit of $\mu_{\text{H}_2\text{O}}$ is $\sim 10^{-5.5}$; This solution retrieves values consistent with those for Mars in our forward models presented in the middle panel of Figure 6.

Table 2. Best-fit parameters for the retrievals with fixed x_{CO_2}

Symbol	x_{CO_2}			
	1	10^{-2}	10^{-4}	10^{-6}
$R_p [R_\oplus]$	1.406	1.0375	1.0378	1.0396
$T [\text{K}]$	158	172	209	232
$\log \kappa_s$	-1.9	-2.5	-3.37	-4.4
s	-0.35	-0.11	-0.098	-0.095
$\log \mu_{\text{H}_2\text{O}}$	-5.4	-6.5	-7.6	-8.7
$\log r_{\text{eff}} [\text{cm}]$	-8.0	-5.8	-5.6	-5.2
$\log \sigma_{\text{r}}$	0.83	0.55	0.51	0.45

To investigate this degeneracy in more detail, best-fit spectra assuming fixed CO_2 mixing ratios (1, 10^{-2} , 10^{-4} , and 10^{-6}) are obtained and shown in Figure 10. The corresponding best-fit parameters are listed in Table 2. While the detailed spectral shapes vary slightly, all models reproduce the observations equally well given the current level of data accuracy. Table 2 clearly shows that synchronized changes in the CO_2 and H_2O mixing ratios, as well as in κ_s , act to preserve the relative strengths of the spectral features. The increasing temperatures at lower CO_2 mixing ratios likely serve to reduce the discrepancy around 2.75–2.95 μm , as demonstrated by the red dashed line in Figure 10, which corresponds to the best-fit solution at $x_{\text{CO}_2} = 10^{-4}$ with a fixed temperature of 150 K. The planetary radius is adjusted to match the absolute level of the transit depth. Small molecular mixing ratios tend to be compensated by a larger planetary radius, except in the case of $x_{\text{CO}_2} = 1$, where the increased mean molecular weight reduces the scale height and thus requires a larger planetary radius at the reference pressure. Constraining the predominance of CO_2 in the atmosphere will require data with higher accuracy and spectral resolution.

As mentioned above, the required noise level as low as 3 ppm is likely too demanding even for the state-of-the-art observations with JWST. It should be noted that the challenge is due in part to the presence of dust particles, rather than the direct effect of the low atmospheric pressure (as might be initially speculated). A simple dust-free CO_2 100% atmosphere with a Mars-like surface pressure (6 mbar) would have more than 3 times larger signal (see Figure 6), enabling the detection of CO_2 with higher noise level.

While the result for TRAPPIST-1f is shown here, the expected signal (and hence the required noise level for detection) for other TRAPPIST-1 planets can be scaled by $R_X h_X$ with equation (5) for h_X . Specifically, based on the planetary parameters given in Agol et al. (2021) ($M_{\text{T1d}} = 0.388M_\oplus$, $R_{\text{T1d}} = 0.788R_\oplus$, $S_{\text{T1d}} = 1.115S_\oplus$, $M_{\text{T1e}} = 0.692M_\oplus$, $R_{\text{T1e}} = 0.92R_\oplus$, $S_{\text{T1d}} = 0.646S_\oplus$) and assuming equal albedos, the signals of TRAPPIST-1d and TRAPPIST-1e are \sim 1.5 times and \sim 1.2 times that of TRAPPIST-1f.

5. DISCUSSIONS

5.1. Temporal variability of molecular features

One of the distinct features in the empirical transit spectra of Mars is the temporal variation in the depth of the CO_2 absorption band at 2.7–2.8 μm driven by the planet’s dust cycle. Could similar variability in transit spectra be expected for rocky planets orbiting M-type stars? A difference from Mars is that exoplanets are observed only at a fixed orbital phase—that is, the same season. Thus, the seasonal variations demonstrated in this study may not appear directly relevant to such targets. However, multi-year observations of Mars have revealed that dust activity can vary significantly from year to year, even during the same season. For

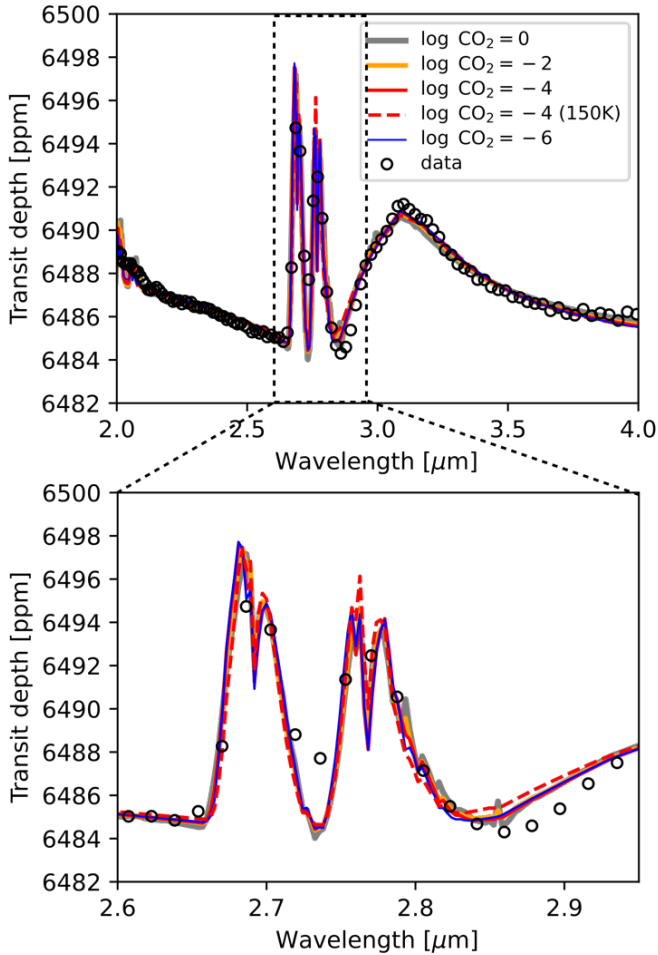


Figure 10. The best-fit solutions for the noise-free transit spectra of “Equinox” with fixed CO_2 mass mixing ratios to 10^{-6} , 10^{-2} , and 1.

example, large-scale, planet-encircling dust storms occur irregularly, approximately once every five Martian years (e.g., Montabone et al. 2015). If similar intermittent dust storms occur on rocky exoplanets, they may contribute to temporal variability in transit spectra.

It should be noted that the processes that causes the time variability of transit spectra does not necessarily involve dust storms. Significant temporal variations in aerosol extinction above the cloud layer have also been observed on Venus (Wilquet et al. 2012). A Mars-like dusty thin atmosphere could be identified by further constraining the dust composition to silicates, for example, through the $10\text{ }\mu\text{m}$ silicate absorption feature (e.g., Ruff & Christensen 2002; Toon et al. 2019).

5.2. $3.1\text{ }\mu\text{m}$ H_2O ice feature

The presence of a H_2O ice signature in transit spectra is intriguing, since H_2O ice on Mars is not typically recognized as one of the most prominent spectroscopic features of the planet. As discussed in Section 3, this feature is attributed to sub-micron-sized mesospheric H_2O ice clouds. Do similar small H_2O cloud particles form on rocky exoplanets in other systems? Put differently, what conditions on exoplanets allow such small cloud particles to form and build up sufficient optical thickness? Understanding the conditions under which small H_2O cloud particles can form is important because it directly informs what we can

infer about an exoplanet when the $3.1\text{ }\mu\text{m}$ feature is detected. Insights into these questions can be gained from the formation processes and environmental conditions of analogous clouds on Solar System planets. Therefore, in what follows, we review the current understanding of H_2O ice clouds on terrestrial planets in the Solar System, and discuss what the detection of such a feature would imply in the context of exoplanet characterization.

Earth also has mesospheric clouds, called noctilucent clouds (NLCs) or polar mesospheric clouds (PMCs). They occur around $\sim 1\text{ Pa}$, a pressure similar to that of Mars' mesosphere but corresponding to altitudes of $80\text{--}85\text{ km}$, in the summer high latitudes. The typical particle size of Earth's mesospheric H_2O clouds is also $< 0.1\text{ }\mu\text{m}$ (e.g., [Rusch et al. 1991](#)), small enough to exhibit the $3.1\text{ }\mu\text{m}$ characteristics in principle. However, empirical transit spectra of Earth do not show such a feature ([Doshi et al. 2022](#)). The cause is uncertain, but possibly due to the small optical depth as well as localization in space and time. There have been no reports of H_2O ice clouds observed in the Venusian atmosphere. Past observations suggested that the atmospheric temperatures at the cloud layer that consists primarily of sulfuric acid droplets (45–70 km) through the aerosol layer (up to 90 km) ([Titov et al. 2018](#)) are too warm to allow for the formation of ice clouds. However, recent studies by [Murray et al. \(2023\)](#) have provided new insights; based on the temperature profiles obtained by the Solar Occultation in the InfraRed (SOIR) instrument onboard the Venus Express spacecraft ([Mahieux et al. 2015, 2023](#)), they noted that temperatures at higher altitudes, around 120 km, could fall to as low as 120 K. At such low temperatures, the formation of ice clouds becomes possible. They suggested that nanometer-scale amorphous solid water (ASW) particles could form across all latitudes under these conditions, and that CO_2 ice particles might condense on ASW surfaces at high latitudes, where temperatures are even lower. Such mesospheric clouds on Venus have not yet been observed, and their existence remains a subject for future investigation.

Formation of mesospheric clouds on both Mars and Earth requires the partial pressure of water vapor reaching the saturation vapor pressure, which depends on the water vapor profiles and the temperature structure. The more limited extent of Earth's mesospheric clouds compared to Mars' may be attributed to the presence of a temperature minimum near the 0.1 bar level, which constrains the water vapor abundance below the saturation pressure at that pressure level ("cold trap", e.g., [Catling & Kasting 2017](#)). Due to this bottle neck in the water vapor transport, along with the relatively warm stratospheric temperature due to O_3 , the atmosphere above the temperature minimum tends to remain under-saturated. This is also the case during the northern summer season on Mars, when relatively low atmospheric temperatures confine water vapor to altitudes below approximately 15–20 km (e.g., [Aoki et al. 2022](#)). This altitude is commonly referred to as the "hygropause". In contrast, mesospheric H_2O clouds on Mars form during the southern summer season when water vapor is efficiently transported upward through the heated lower atmosphere (e.g., [Aoki et al. 2022](#)). Thus, the prominent presence of mesospheric H_2O clouds may reflect key aspects of the underlying atmospheric structure, in particular, the absence of cold trap or hygropause.

Furthermore, studies on the mesospheric clouds on Mars and Earth have highlighted the importance of the availability of cloud condensation nuclei (CCN). The formation PMCs on Earth likely involves heterogeneous nucleation on dust grains produced by meteoric ablation (e.g., [Tanaka et al. 2022](#)). Similarly, theoretical studies suggest that Martian mesospheric H_2O ice clouds preferentially form via heterogeneous nucleation, either on dust particles lofted from the lower atmosphere (e.g., [Määttänen et al. 2005](#)), or on exogenous dust grains originating from meteoric ablation (e.g., [Hartwick et al. 2019](#)). Accordingly, the detection of mesospheric clouds on exoplanets may point to analogous processes that supply CCN in their upper atmospheres, such as the influx of micrometeoroids or the vertical transport of dust.

It should be noted that H_2O ice clouds can also form below the mesosphere. Indeed, Earth has H_2O ice clouds in the upper troposphere and stratosphere. Clouds in the upper troposphere, which include familiar types of clouds such as cirrus, cirrostratus, and cirrocumulus, form when moist air ascends and cools. Stratospheric H_2O ice clouds are rarer and typically form over polar regions during winter known as Polar Stratospheric Cloud (PSC), when the air is substantially cooled. The $3.1\text{ }\mu\text{m}$ feature from these clouds is again absent in empirical transit spectra of Earth (Doshi et al. 2022). This is likely due (at least in part) to the particle sizes. Typical particle sizes of clouds in the upper troposphere and stratosphere are tens of microns (e.g., Liou 1986) and $2\text{--}10\text{ }\mu\text{m}$ (e.g., Dye et al. 1992), respectively. These sizes are too large to clearly exhibit the $3.1\text{ }\mu\text{m}$ feature (Figure 9), and such clouds contribute to the transit spectra primarily as gray opacity. In the water-rich environment of Earth’s lower atmosphere, cloud particles can grow in a relatively short timescale, until they become large enough to even more rapidly grow through coalescence and/or fall (e.g., Rossow 1978).

Whether or not exoplanets develop H_2O clouds with a sufficient slant optical depth at $3.1\text{ }\mu\text{m}$ depends ultimately on the interplay among water vapor transport, heat transport, and transport of CCN via atmospheric dynamics—processes that are difficult to accurately model. Fauchez et al. (2019) who used a general circulation model (GCM) to simulate the atmospheres of TRAPPIST-1 planets suggested the presence of H_2O ice clouds at the terminator with particle sizes of approximately $2\text{ }\mu\text{m}$. However, cloud particle sizes depend on both the number density of CCN and the details of atmospheric circulation, introducing significant modeling uncertainties. Similarly, the formation of mesospheric H_2O ice clouds on exoplanets is influenced by the availability of CCN, the water vapor content, and the local thermal structure—often modulated by atmospheric wave activity—making their occurrence probability uncertain. To the best of our knowledge, the existence of mesospheric clouds on exoplanets has not been explicitly addressed in the literature. Whether, and under what conditions, such H_2O ice clouds form and retain small particle sizes remains an open question.

Nevertheless, it should be noted if such sub-micron-sized H_2O ice clouds do form, the $3.1\text{ }\mu\text{m}$ H_2O ice absorption feature is substantially more stronger than the low-resolution H_2O *vapor* bands for a given water mass mixing ratio. Therefore, it would serve as a valuable compositional clue in future atmospheric characterization of habitable-zone exoplanets.

6. SUMMARY

This study analyzes the empirical transit spectra of Mars, reconstructed from solar occultation measurements by the NOMAD instrument onboard the ExoMars Trace Gas Orbiter, to investigate how a Mars-like surface environment on exoplanets would be seen in transit observations. The results show that Mars’ lower atmosphere is largely opaque below $\sim 25\text{ km}$ ($\sim 0.5\text{ mbar}$) due to the presence of dust and H_2O ice clouds, while the $2.7\text{--}2.8\text{ }\mu\text{m}$ CO_2 absorption band and distinct $3.1\text{ }\mu\text{m}$ H_2O ice features are identified. These spectral features exhibit marked seasonal variability: during dusty periods, the $2.7\text{--}2.8\text{ }\mu\text{m}$ CO_2 absorption weakens, and the H_2O ice feature at $3.1\text{ }\mu\text{m}$ becomes more prominent. Forward modeling with PSG shows that the empirical spectra are well reproduced when vertical atmospheric structures based on previous observational studies are incorporated. Aerosols, particularly dust and fine ice particles, strongly influence both the continuum slope and the amplitude of spectral features.

The $3.1\text{ }\mu\text{m}$ H_2O feature is intriguing given the low abundance of water vapor on Mars. This is attributed to the sub-micron-sized mesospheric H_2O clouds formed above 40 km in altitude ($\sim 0.1\text{ mbar}$). This spectral feature of H_2O is sensitive to small mass mixing ratio of water, and could be a sensitive indicator of the presence of water in cold, arid atmospheres like that of Mars, where water *vapor* absorption cannot be

detected. The large spatial extent of mesospheric water clouds with small ice particles as observed for Mars (and has not been observed on Earth) is likely related to certain properties of Mars, including no prominent cold trap and airborne dust particles that efficiently heat the lower atmosphere. These findings highlight the diagnostic potential of aerosol- and cloud-related features for characterizing the atmospheric environments of terrestrial exoplanets. However, it should also be noted that uniquely identifying a planet’s climate state from transmission spectra over a limited wavelength range remains a significant challenge. Such an inference likely requires multi-faceted characterization using various observational techniques, with transmission spectral properties serving as one piece of evidence.

To evaluate the detectability of such features in an exoplanetary context, we simulate transit observations of a Mars-like atmosphere scaled to TRAPPIST-1f and perform retrieval analysis. Our results indicate that both CO₂ and H₂O ice features can be detected at precisions better than ~ 3 ppm. However, absolute abundance estimates are limited by uncertainties in the reconstructed transit spectra, coupled with degeneracies involving planetary radius and reference pressure. The required precision exceeds current technological capabilities, demonstrating the challenge of characterizing dusty atmospheres like Mars.

Our analysis adds to the limited sample of empirical transit spectra of well-studied solar system planets—Earth (Macdonald & Cowan 2019; Doshi et al. 2022) and Titan (Robinson et al. 2014). Given the difficulty of accurately modeling three-dimensional atmospheric properties, particularly those involving aerosols and dust, these empirical spectra serve as valuable benchmarks for future exoplanet investigations.

ACKNOWLEDGMENTS

We greatly thank Kazumasa Ohno for the insightful discussions on the cloud properties and their impact on transit spectra. We also thank Tatsuya Yoshida for valuable discussions on the implications of Martian dust for the planet’s evolutionary history.

SA was supported by JSPS KAKENHI Grant Number 24K21565, 22K03709, 22H05151, 22H00164, and 22KK0044. YF was supported by JSPS KAKENHI Grant Number 18K13601. GLV was supported by NASA’s Mars Program Office under “GSFC participation in the TGO/NOMAD Investigation of Trace Gases on Mars” and by NASA’s SEEC Exoplanetary collaboration.

The NOMAD experiment is led by the Royal Belgian Institute for Space Aeronomy (IASB-BIRA) with co-PI teams from Spain (IAA-CSIC), Italy (INAF-IAPS) and the United Kingdom (Open University). This project acknowledges funding by: the Belgian Science Policy Office (BELSPO) with the financial and contractual coordination by the ESA Prodex Office (PEA 4000103401, 4000121493, 4000140753, 4000140863); by the Spanish Ministry of Science and Innovation (MCIU) and European funds (grants PGC2018-101836-B-I00 and ESP2017-87143-R; MINECO/FEDER), from the Severo Ochoa (CEX2021-001131-S) and from MCIN/AEI/10.13039/501100011033 (grants PID2022-137579NB-I00, RTI2018-100920-J-I00 and PID2022-141216NB-I00); by the UK Space Agency (grants ST/V002295/1, ST/V005332/1, ST/X006549/1, ST/Y000234/1 and ST/R003025/1); and by the Italian Space Agency (grant 2018-2-HH.0).

Software: petitRADTRANS (Mollière et al. 2019), Planetary Spectrum Generator (Villanueva et al. 2018)

REFERENCES

Agol, E., Dorn, C., Grimm, S. L., et al. 2021, PSJ, 2, 1, doi: [10.3847/PSJ/abd022](https://doi.org/10.3847/PSJ/abd022)

Aoki, S., Vandaele, A. C., Daerden, F., et al. 2022, Journal of Geophysical Research (Planets), 127, e07231, doi: [10.1029/2022JE007231](https://doi.org/10.1029/2022JE007231)

Aoki, S., Faggi, S., Villanueva, G. L., et al. 2024, PSJ, 5, 158, doi: [10.3847/PSJ/ad58dc](https://doi.org/10.3847/PSJ/ad58dc)

Barclay, T., Sheppard, K. B., Latouf, N., et al. 2025, AJ, 169, 241, doi: [10.3847/1538-3881/ada5f6](https://doi.org/10.3847/1538-3881/ada5f6)

Benneke, B., & Seager, S. 2012, ApJ, 753, 100, doi: [10.1088/0004-637X/753/2/100](https://doi.org/10.1088/0004-637X/753/2/100)

Catling, D. C., & Kasting, J. F. 2017, Atmospheric Evolution on Inhabited and Lifeless Worlds

Changeat, Q., Bardet, D., Chubb, K., et al. 2025, arXiv e-prints, arXiv:2505.18715, doi: [10.48550/arXiv.2505.18715](https://doi.org/10.48550/arXiv.2505.18715)

Clancy, R. T., Wolff, M. J., Smith, M. D., et al. 2019, Icarus, 328, 246, doi: [10.1016/j.icarus.2019.03.025](https://doi.org/10.1016/j.icarus.2019.03.025)

Clapp, M. L., Worsnop, D. R., & Miller, R. E. 1995, Journal of physical chemistry, 99, 6317

Doshi, D., Cowan, N. B., & Huang, Y. 2022, MNRAS, 515, 1982, doi: [10.1093/mnras/stac1869](https://doi.org/10.1093/mnras/stac1869)

Dye, J. E., Baumgardner, D., Gandrud, B. W., et al. 1992, J. Geophys. Res., 97, 8015, doi: [10.1029/91JD02740](https://doi.org/10.1029/91JD02740)

Fauchez, T. J., Turbet, M., Villanueva, G. L., et al. 2019, ApJ, 887, 194, doi: [10.3847/1538-4357/ab5862](https://doi.org/10.3847/1538-4357/ab5862)

Fedorova, A. A., Montmessin, F., Rodin, A. V., et al. 2014, Icarus, 231, 239, doi: [10.1016/j.icarus.2013.12.015](https://doi.org/10.1016/j.icarus.2013.12.015)

Fortney, J. J. 2005, MNRAS, 364, 649, doi: [10.1111/j.1365-2966.2005.09587.x](https://doi.org/10.1111/j.1365-2966.2005.09587.x)

Fujii, Y., Del Genio, A. D., & Amundsen, D. S. 2017, ApJ, 848, 100, doi: [10.3847/1538-4357/aa8955](https://doi.org/10.3847/1538-4357/aa8955)

Fujii, Y., Angerhausen, D., Deitrick, R., et al. 2018, Astrobiology, 18, 739, doi: [10.1089/ast.2017.1733](https://doi.org/10.1089/ast.2017.1733)

Gordon, I. E., Rothman, L. S., Hargreaves, R. J., et al. 2022, JQSRT, 277, 107949, doi: [10.1016/j.jqsrt.2021.107949](https://doi.org/10.1016/j.jqsrt.2021.107949)

Hartwick, V. L., Toon, O. B., & Heavens, N. G. 2019, Nature Geoscience, 12, 516, doi: [10.1038/s41561-019-0379-6](https://doi.org/10.1038/s41561-019-0379-6)

Heavens, N. G., Richardson, M. I., Kleinböhl, A., et al. 2011, Journal of Geophysical Research (Planets), 116, E01007, doi: [10.1029/2010JE003692](https://doi.org/10.1029/2010JE003692)

Heng, K., & Kitzmann, D. 2017, MNRAS, 470, 2972, doi: [10.1093/mnras/stx1453](https://doi.org/10.1093/mnras/stx1453)

Holmberg, M., & Madhusudhan, N. 2024, A&A, 683, L2, doi: [10.1051/0004-6361/202348238](https://doi.org/10.1051/0004-6361/202348238)

Jeffreys, H. 1939, Theory of Probability

Kaltenegger, L., & Traub, W. A. 2009, ApJ, 698, 519, doi: [10.1088/0004-637X/698/1/519](https://doi.org/10.1088/0004-637X/698/1/519)

Kopparapu, R. k., Wolf, E. T., Arney, G., et al. 2017, ApJ, 845, 5, doi: [10.3847/1538-4357/aa7cf9](https://doi.org/10.3847/1538-4357/aa7cf9)

Lecavelier Des Etangs, A., Pont, F., Vidal-Madjar, A., & Sing, D. 2008, A&A, 481, L83, doi: [10.1051/0004-6361:200809388](https://doi.org/10.1051/0004-6361:200809388)

Lefèvre, F., Trokhimovskiy, A., Fedorova, A., et al. 2021, Journal of Geophysical Research (Planets), 126, e06838, doi: [10.1029/2021JE006838](https://doi.org/10.1029/2021JE006838)

Lim, O., Benneke, B., Doyon, R., et al. 2023, ApJL, 955, L22, doi: [10.3847/2041-8213/acf7c4](https://doi.org/10.3847/2041-8213/acf7c4)

Liou, K.-N. 1986, Monthly Weather Review, 114, 1167, doi: [10.1175/1520-0493\(1986\)114<1167:IOCCOW>2.0.CO;2](https://doi.org/10.1175/1520-0493(1986)114<1167:IOCCOW>2.0.CO;2)

Liuzzi, G., Villanueva, G. L., Crismani, M. M. J., et al. 2020, Journal of Geophysical Research (Planets), 125, e06250, doi: [10.1029/2019JE006250](https://doi.org/10.1029/2019JE006250)

Liuzzi, G., Villanueva, G., Aoki, S., et al. 2024, in EGU General Assembly Conference Abstracts, EGU General Assembly Conference Abstracts, 17142, doi: [10.5194/egusphere-egu24-17142](https://doi.org/10.5194/egusphere-egu24-17142)

Määttänen, A., Vehkämäki, H., Lauri, A., et al. 2005, Journal of Geophysical Research (Planets), 110, E02002, doi: [10.1029/2004JE002308](https://doi.org/10.1029/2004JE002308)

Macdonald, E. J. R., & Cowan, N. B. 2019, MNRAS, 489, 196, doi: [10.1093/mnras/stz2047](https://doi.org/10.1093/mnras/stz2047)

Madhusudhan, N., Constantinou, S., Holmberg, M., et al. 2025, ApJL, 983, L40, doi: [10.3847/2041-8213/adc1c8](https://doi.org/10.3847/2041-8213/adc1c8)

Mahieux, A., Robert, S., Piccialli, A., Trompet, L., & Vandaele, A. C. 2023, Icarus, 405, 115713, doi: [10.1016/j.icarus.2023.115713](https://doi.org/10.1016/j.icarus.2023.115713)

Mahieux, A., Vandaele, A. C., Bouger, S. W., et al. 2015, Planet. Space Sci., 113, 309, doi: [10.1016/j.pss.2015.02.002](https://doi.org/10.1016/j.pss.2015.02.002)

Mason, J. P., Patel, M. R., Leese, M. R., et al. 2022, Planet. Space Sci., 218, 105432, doi: [10.1016/j.pss.2022.105432](https://doi.org/10.1016/j.pss.2022.105432)

Millour, E., Forget, F., Spiga, A., et al. 2018, in From Mars Express to ExoMars, 68

Mollière, P., Wardenier, J. P., van Boekel, R., et al. 2019, A&A, 627, A67, doi: [10.1051/0004-6361/201935470](https://doi.org/10.1051/0004-6361/201935470)

Montabone, L., Forget, F., Millour, E., et al. 2015, *Icarus*, 251, 65, doi: [10.1016/j.icarus.2014.12.034](https://doi.org/10.1016/j.icarus.2014.12.034)

Montmessin, F., Forget, F., Rannou, P., Cabane, M., & Haberle, R. M. 2004, *Journal of Geophysical Research (Planets)*, 109, E10004, doi: [10.1029/2004JE002284](https://doi.org/10.1029/2004JE002284)

Murray, B. J., Mangan, T. P., Määttänen, A., & Plane, J. M. C. 2023, *Journal of Geophysical Research (Planets)*, 128, e2023JE007974, doi: [10.1029/2023JE0079741.22541/essoar.168881878.84423936/v1](https://doi.org/10.1029/2023JE0079741.22541/essoar.168881878.84423936/v1)

Neefs, E., Vandaele, A. C., Drummond, R., et al. 2015, *ApOpt*, 54, 8494, doi: [10.1364/AO.54.008494](https://doi.org/10.1364/AO.54.008494)

Patel, M. R., Antoine, P., Mason, J., et al. 2017, *ApOpt*, 56, 2771, doi: [10.1364/ao.56.002771](https://doi.org/10.1364/ao.56.002771)

Patel, M. R., Sellers, G., Mason, J. P., et al. 2021, *Journal of Geophysical Research (Planets)*, 126, e06837, doi: [10.1029/2021JE006837](https://doi.org/10.1029/2021JE006837)

Robinson, T. D., Maltagliati, L., Marley, M. S., & Fortney, J. J. 2014, *Proceedings of the National Academy of Science*, 111, 9042, doi: [10.1073/pnas.1403473111](https://doi.org/10.1073/pnas.1403473111)

Rossow, W. B. 1978, *Icarus*, 36, 1, doi: [10.1016/0019-1035\(78\)90072-6](https://doi.org/10.1016/0019-1035(78)90072-6)

Ruff, S. W., & Christensen, P. R. 2002, *Journal of Geophysical Research (Planets)*, 107, 5127, doi: [10.1029/2001JE001580](https://doi.org/10.1029/2001JE001580)

Rusch, D. W., Thomas, G. E., & Jensen, E. J. 1991, *J. Geophys. Res.*, 96, 12,933, doi: [10.1029/91JD01227](https://doi.org/10.1029/91JD01227)

Schreier, F., Städter, S., Hedelt, P., & Godolt, M. 2018, *Molecular Astrophysics*, 11, 1, doi: <https://doi.org/10.1016/j.molap.2018.02.001>

Smith, M. D. 2008, *Annual Review of Earth and Planetary Sciences*, 36, 191, doi: [10.1146/annurev.earth.36.031207.124334](https://doi.org/10.1146/annurev.earth.36.031207.124334)

Smith, R. G., Robinson, G., Hyland, A. R., & Carpenter, G. L. 1994, *MNRAS*, 271, 481, doi: [10.1093/mnras/271.2.481](https://doi.org/10.1093/mnras/271.2.481)

Stcherbinine, A., Montmessin, F., Vincendon, M., et al. 2022, *Journal of Geophysical Research (Planets)*, 127, e2022JE007502, doi: [10.1029/2022JE007502](https://doi.org/10.1029/2022JE007502)

Stolzenbach, A., López Valverde, M.-A., Brines, A., et al. 2023a, *Journal of Geophysical Research (Planets)*, 128, e2023JE007835, doi: [10.1029/2023JE007835](https://doi.org/10.1029/2023JE007835)

—. 2023b, *Journal of Geophysical Research (Planets)*, 128, e2023JE007835, doi: [10.1029/2023JE007835](https://doi.org/10.1029/2023JE007835)

Tanaka, K. K., Mann, I., & Kimura, Y. 2022, *Atmospheric Chemistry and Physics*, 22, 5639, doi: [10.5194/acp-22-5639-2022](https://doi.org/10.5194/acp-22-5639-2022)

Titov, D. V., Ignatiev, N. I., McGouldrick, K., Wilquet, V., & Wilson, C. F. 2018, *SSRv*, 214, 126, doi: [10.1007/s11214-018-0552-z](https://doi.org/10.1007/s11214-018-0552-z)

Toon, G. C., Liebe, C. C., Nemati, B., et al. 2019, *Earth and Space Science*, 6, 836, doi: [10.1029/2018EA000469](https://doi.org/10.1029/2018EA000469)

Vandaele, A. C., Lopez-Moreno, J. J., Patel, M. R., et al. 2018, *SSRv*, 214, 80, doi: [10.1007/s11214-018-0517-2](https://doi.org/10.1007/s11214-018-0517-2)

Villanueva, G. L., Smith, M. D., Protopapa, S., Faggi, S., & Mandell, A. M. 2018, *JQSRT*, 217, 86, doi: [10.1016/j.jqsrt.2018.05.023](https://doi.org/10.1016/j.jqsrt.2018.05.023)

Villanueva, G. L., Liuzzi, G., Crismani, M. M. J., et al. 2021, *Science Advances*, 7, eabc8843, doi: [10.1126/sciadv.abc8843](https://doi.org/10.1126/sciadv.abc8843)

Warren, S. G., & Brandt, R. E. 2008, *Journal of Geophysical Research (Atmospheres)*, 113, D14220, doi: [10.1029/2007JD009744](https://doi.org/10.1029/2007JD009744)

Willame, Y., Depiesse, C., Mason, J. P., et al. 2022, *Planet. Space Sci.*, 218, 105504, doi: [10.1016/j.pss.2022.105504](https://doi.org/10.1016/j.pss.2022.105504)

Wilquet, V., Drummond, R., Mahieux, A., et al. 2012, *Icarus*, 217, 875, doi: [10.1016/j.icarus.2011.11.002](https://doi.org/10.1016/j.icarus.2011.11.002)

Wolff, M. J., Smith, M. D., Clancy, R. T., et al. 2009, *Journal of Geophysical Research (Planets)*, 114, E00D04, doi: [10.1029/2009JE003350](https://doi.org/10.1029/2009JE003350)

Yurchenko, S. N., Mellor, T. M., Freedman, R. S., & Tennyson, J. 2020, *MNRAS*, 496, 5282, doi: [10.1093/mnras/staa1874](https://doi.org/10.1093/mnras/staa1874)